C. Karmonik, Ph.D.

COMPUTATIONAL FLUID DYNAMICS AS A TOOL FOR VISUALIZING HEMODYNAMIC FLOW PATTERNS

Christof Karmonik, Ph.D.; Jean Bismuth, M.D.; Mark G. Davies, M.D., Ph.D., M.B.A.; Alan B. Lumsden, M.D.

Methodist DeBakey Heart & Vascular Center, Houston, Texas; Weill Medical College of Cornell University, New York, New York; The Methodist Hospital Neurological Institute, Houston, Texas

Abstract

Computational fluid dynamics (CFD) techniques have progressed to a point where they can be routinely applied towards the simulation of blood flow dynamics in the human vasculature. Patient-specific geometries and physiologically accurate flow rates can be obtained from clinical images to provide accurate boundary conditions for these simulations. Advances in computer hardware and CFD software in recent years have reduced the simulation computing time from days to hours. Such a time frame permits incorporation of the information obtained with CFD into the clinical workflow for the surgical repair of vascular pathologies. In this article, the concepts of CFD are introduced via a patient-specific simulation of the hemodynamics in a type III B aortic dissection. Emphasis is placed on the practical aspects of how to optimize CFD simulations so that their results may be of clinical value to the treating surgeon. Limitations as they exist today are discussed.

Introduction

Advances in many areas of medical research have led to the concept of personalized medicine. As described in the overview section of the National Heart Lung and Blood Institute's Strategic Plan of the Division of Cardiovascular Diseases, "Personalized medicine uses enabling technologies, along with clinical and environmental information about an individual, to tailor prevention, management, or treatment of a disease or condition for that individual. These technologies include genetics, genomics, proteomics, and other 'omics and bioengineering approaches. Barriers may include timely translation of research findings, as well as a dearth of identification of molecular markers with proven clinical benefit, clinical trials, and application to clinical practice. Novel research and translational strategies are needed to facilitate widespread use of personalized medicine in the clinic."[21]

While computational simulations in general, and simulations of blood flow in human arteries in particular, have been the topic of research in the last decades,[22-27] the recent introduction of advanced clinical imaging techniques and improved computing power has make it possible to tailor these simulations towards the conditions found in a particular individual.[28-33] Initially, CFD simulations were restricted to two-dimensional models and idealized geometries, and solutions even for these simplified geometries could only be obtained after many hours or even days. Continuous technical advances, however, have made it possible to convert information from images acquired during a routine clinical exam into three-dimensional complex mathematical meshes consisting of hundreds of thousands of small-volume elements for transient simulation of the hemodynamics in artery segments of the human vasculature, either in a healthy or diseased state.[12,34,35] The results of these simulations provide access to hemodynamic parameters that currently are not reliably measurable with clinical imaging methods.

Arguably, one of the most important of these parameters is the wall shear stress (WSS) that the flowing blood is exerting onto the arterial wall, as endothelial cells have been demonstrated to sense the magnitude and changes in the orientation of the WSS vector. For example, endothelial cells respond to shearing forces caused by time-varying flow, and a WSS magnitude of less than 1.5 Pa will degenerate the arterial wall via the apoptotic cell cycle.[36] Other parameters include dynamic pressures and recirculation patterns; the latter may facilitate the adhesion of material onto the artery wall and promote the creation of atherosclerotic lesions, such as in the bulb of the carotid bifurcation, for example.

In this article, the concept of personalized CFD is illustrated with an example of a type III B aortic dissection (B-AD). Aortic dissections are blood-filled, axial separations between elastic laminae within the media.[3,5] Rupture occurs in about 90% of cases. In 10% of all cases, re-entrant tears into the aortic lumen exist. The false lumen often re-endothelializes, however, and thrombus formation is also often observed.[1]

The algorithms for creating the computational meshes and for calculating the aortic volumetric blood flow rate as inflow conditions for the CFO simulations from the clinical medical images are also presented. The information that can be obtained from the CFD simulations is described, including WSS, dynamic pressures, and blood flow pathlines. The validity of this information is discussed, particularly with respect to the assumptions that are necessary to enable the simulation of such a complex system as the human aorta.

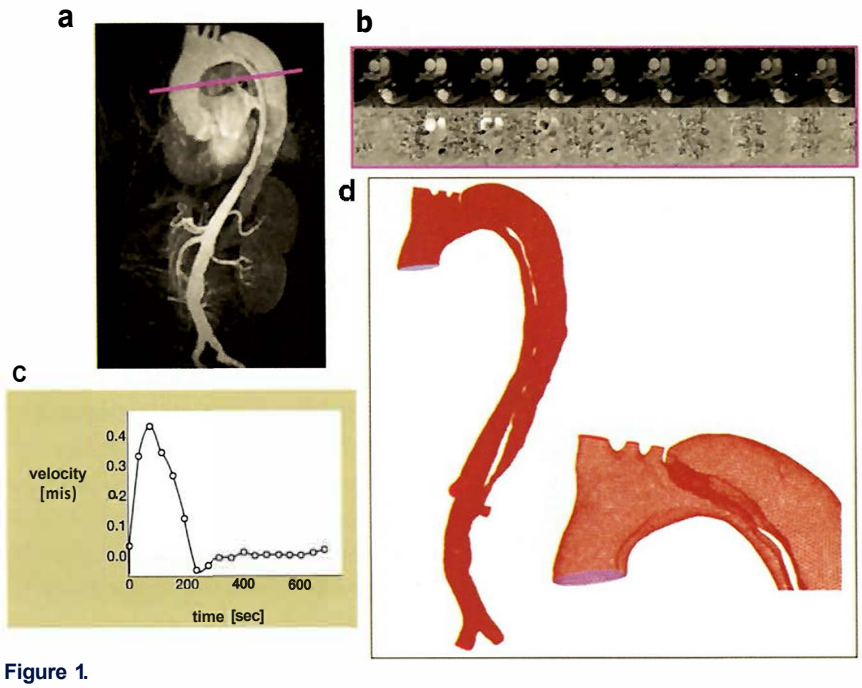

Figure 1.

a) Maximal intensity proiection of the three-dimensional contrast-enhanced MRA images displaying the true and false lumen of this aortic dissection. The line marks the location of the 20 pcMRI image acquisition.

b) 2D pcMRI images (at odd time points). The top row shows magnitude images from which the lumen of the ascending aorta was segmented. The bottom row shows phase images where the gray-scale image intensity is proportional to the velocity of the blood.

c) Aortic velocity waveform derived from the 20 pcMRI images.

d) Computational mesh consisting of 360.275 tetrahedral volume elements. Left: whole computational domain; right: enlarged region with the entrance tear.

Methods

Approval of the institutional review board was obtained for this retrospective study.

Clinical Imaging

A patient with a type ill B dissection whose history was unclear underwent a magnetic resonance imaging (MRI) exam, which included a contrast-enhanced magnetic resonance angiography (ceMRA, sagittal, in-plane resolution 1.04 x 1.04 mm, slice thickness 1.75, one breath hold) of the aorta (Figure la). While computed tomography {CT) or digital subtraction angiography (DSA) are routinely used to assess aortic dissections,[-10] cine magnetic resonance imaging has the advantage to provide physiological information in addition to anatomical images.[13-20] Cine two-dimensional phase contrast magnetic resonance images (20 pcMRI) were acquired in an axial orientation at two locations: at the thoracic aorta (Figure lb, location 1) and the abdominal aorta (location 2) (TR 41 ms, in-plane resolution 1.17 x 1.17 mm, slice thickness 5 mm, one breath hold) using a Siemens Sonata Magnetom 1.5 T human MRI scanner (Siemens, Medical Solutions, Erlangen, Germany). At location 1, the false lumen of the aorta was patent and partly occluded by thrombus at location 2. A velocity encoding value (VENC) of 150 cm/sec as the estimated maximum velocity was selected by the operator to ensure optimum contrast between moving blood in the true aortic lumen and stationary tissue. The cross sections of the ascending aortic in the images from location 1 were used to calculate the aortic volumetric flow rate (Figure lb).

Aortic Volumetric Flow Rate

The magnitude 20 pcMRJ images were filtered with a median filter (ImageJ, NIH).[37] This approach was chosen as the median filter is known to preserve edges in digital image processing.[11,45] In the median filtered images, the lumen of the ascending thoracic aorta exhibited high contrast to stationary tissue and could therefore be segmented by single-value thresholding. Using a single-value region-growing algorithm with a seed placed in the lumen of the ascending aorta, the lumen boundary was extracted and used as a mask in the phase 2D pcMRI images. The average blood flow

velocity in each image was calculated as the average of the pixel values within the aortic lumen. Aortic flow was calculated as the product of this average velocity and the area of the lumen yielding the aortic flow-time curves (Figure le).

Computational Meshes

The 88 contiguous sagittal ceMRA images were filtered with a Fourier bandpass filter (using the JAVA-based image-processing software ImageJ, available from the NIH website) to remove large image grayscale intensity variations (80 voxels or larger) created by the inhomogeneous sensitivity profile of the coil and to suppress small variations (4 voxels or less) created by noise. The surface of the true and false lumen of the aorta was obtained using the single thresholding technique (Figure 1). A stereolithographic file was created from this reconstruction **with** Paraview (www.paraview.org), imported into GAMBIT (ANSYS-Fluent Inc.), and meshed using 360,275 tetrahedral volume elements (Figure ld).

CFD Simulations

Transient CFO simulations with no-slip conditions, rigid walls, and Newtonian properties of the blood (density of 1050 kg/m^3 and a constant viscosity of 0.004 kg/ms) were performed. The Navier-Stokes equations were solved with pressure-based, implicit, three-dimensional double precision, second-order solver (ANSYS- Fluent Inc). Time step length for the simulations was 5 msec. Total length of the cardiac interval was 690 msec, resulting in 138 time steps per cardiac cycle. Total pressures, blood velocities, dynamic pressures, and WSS were determined from these simulations.

Results

Aortic Volumetric Flow Rate

The average span of the cardiac intervals used for the image acquisition was 692 ms. The minimum and maximum blood velocities during this time interval were -0.046 m/s and 0.430 m/s, respectively. The velocity was converted into the flow rate (mL/sec) by taking into consideration the cross section of the aorta where the inflow was measured (8.6 10^{-4} m^2). The average aortic flow rate was 71 mL/sec (-39 -369 mL/sec). Maximum flow occurred at 78 ms, minimum flow at 243 ms (retrograde flow), and antegrade flow was restored at 405 ms (Figure le).

Hemodynamic Flow Patterns

1. Velocity Magnitude

Cross-sectional planes located inside the arterial lumen can be used for visualizing the magnitude of the blood velocity. With this approach, the difference in magnitude of the velocities in the true and false lumen around the entrance tear could be read-

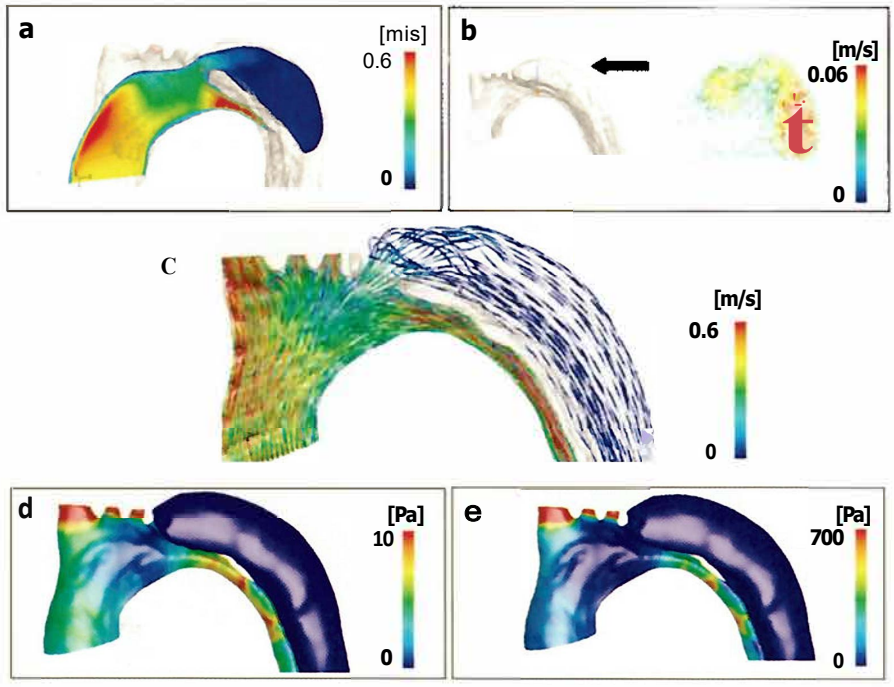

Figure 2.

a) Velocity magnitude displayed on a cross-sectional intersection of the aortic lumen and the entrance tear at the time of maximal inflow. An outline of the computational mesh is shown for orientation purposes.

b) Velocity vectors displayed at a cut plane intersecting the true and false lumen (inset on left) at the time of maximum inflow. Complex secondary flow patterns are readily appreciated.

c) Pathlines originating from the aortic inflow boundary at the time of maximal inflow. Laminar, ordered flow is visible in the aortic lumen proximal to the entrance tear and in the true aortic lumen. In contrast. flow is disturbed immediately distal to the entrance tear in the false lumen, most likely due to flow deceleration.

d) WSS magnitude for maximum inflow at the wall of the computational domain. High values are apparent in the true lumen compared to the false lumen.

e) Dynamic pressure for maximum inflow at the wall of the computational domain. High values are apparent in the true lumen compared to the false lumen.

ily appreciated. Immediately at this location, the blood velocity was about 0.3 m/s; it sharply increased distally to values > 1 m/s in the true lumen and values < 0.03 m/s in the false lumen (Figure 2a).

2. Velocity Vectors

In addition to the magnitude of the blood flow velocity, the directionality of the flow is also of interest, especially for identifying regions of low and recirculating flow. In these regions, secondary flow patterns are present and decelerating forward flow, which may be an indicator for thrombus formation. The deceleration of the blood entering the false lumen resulted in strong secondary flow patterns (Figure 2b), revealing an increasing complexity of hemod$_{y n}$ amics in the false lumen.

3. **Pathlines** of Flow

Pathlines can be used to visualize the flow directions in an entire volume. With this technique, laminar flow was identified in the aorta proximal and distal to the entrance tear into the false lumen. In the false lumen, in a region immediately distal to the entrance tear, pathlines revealed disordered flow consistent with the secondary flow patterns observed at this location. Beyond this region, the flow resumed an ordered, laminar structure (Figure 2c).

4. WSS Magnitude

The WSS magnitude is of particular interest as it represents a hemodynamic parameter that exerts a force on the aortic wall dependent on the gradient of the velocity normal to the wall per unit area. WSS magnitude was elevated in the true aortic lumen immediately distal to the entrance. A reduction of the aortic cross section created higher blood flow velocities in the center of the lumen and consequently created a larger velocity gradient normal to the wall. In the false lumen, the opposite effect was observed with an enlarged luminal cross section (Figure 2d).

5. Dynamic Pressure

As for the WSS magnitude, the force that creates the dynamic pressure has its origin in the flowing blood. While **in** the case of the WSS magnitude this force is oriented in line with the wall segment, for the dynamic pressure it is always oriented perpendicular to this segment. For the B-AD, the spatial distribution of WSS magnitude and dynamic pressure were similar on the arterial wall: both were elevated **in** the true lumen distal to the location of the entrance tear and decreased **in** the false lumen (Figure 2e).

6. Total Pressure

The total pressure represents the pressure that would be measured, e.g., by a pressure catheter inserted in the aortic lumen. The total pressure was elevated in the false lumen by about a factor of 10 (95 Pa) compared to the true lumen (about 10 Pa). This difference most likely was caused by a large reduction of the cross-sectional area of the false aortic lumen just proximal to the reentrant tear (Figure 3).

7. Time-Averaged WSS

In addition to analyzing the values of the hemodynamic parameters at different times, time-averaged values can also be evaluated. For instance, for the WSS magnitude a temporal mean and a standard deviation can be obtained from the instantaneous WSS values for each time point. The time-averaged WSS magnitude (<WSS>) did not differ significantly from the WSS magnitude at maximal inflow (Figure 2d and Figure 4a). Large variations as represented by the standard deviation of the WSS (WSS) were found proximal to the

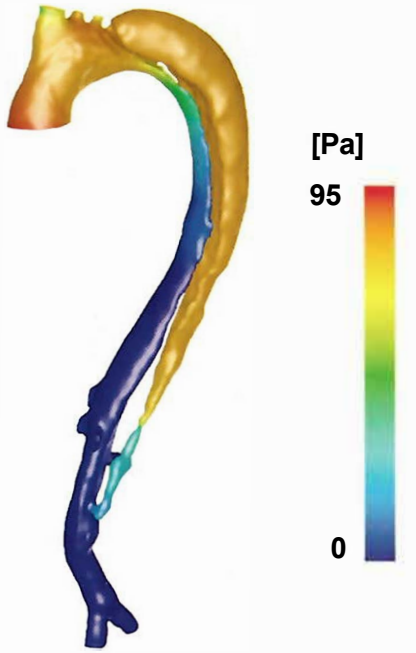

Figure 3.
Three-dimensional surface reconstruction of the whole computational domain colored by the total pressure according to the displayed color legend. Total pressure in the false lumen is about an order ol magnitude larger than in the true lumen.

entrance tear into the false **lumen** (Figure 4c).

8. Oscillatory Shear Index (OSI)

The OSI is a measure for variation in direction of the WSS vector.[38] It therefore complements the WSS magnitude, which represents the magnitude of this vector. Large values for the OSI were found at the wall of the false lumen but also at the posterior aortic wall proximal to the entrance tear (Figure 4d). For all of these areas, the time-averaged WSS magnitude was also low (Figure 4a).

9. Unsteady Solution

In addition to transient CFD simulations, a steady simulation can also be performed in which the inflow velocity is kept constant. The temporal average is usually chosen for this constant. A WSS magnitude also can be calculated

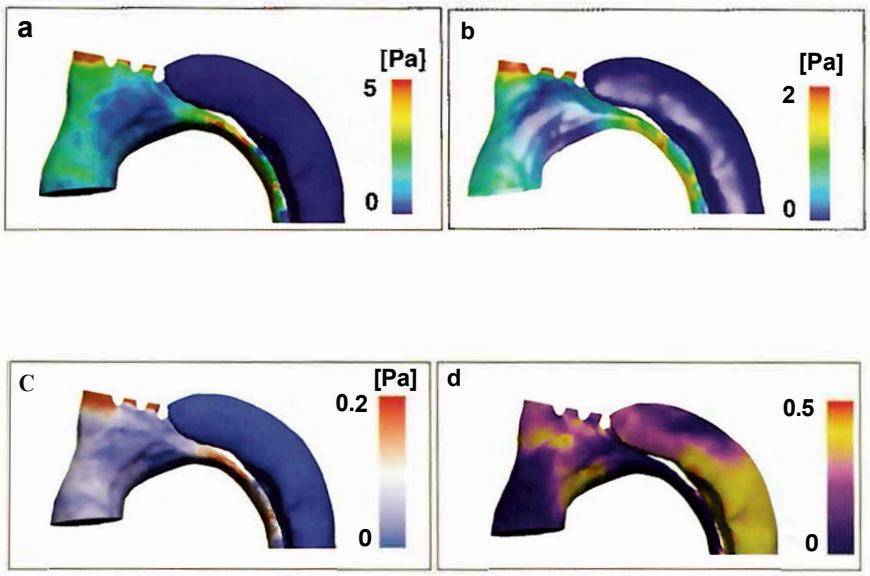

Figure 4.

a) Time-averaged WSS magnitude on the aortic wall. Spatial distribution is similar to the WSS magnitude at maximum inflow, but absolute values are decreased.

b} WSS magnitude obtained from a steady simulation. Spatial distribution is similar to the WSS magnitude at maximum inflow, but absolute values are decreased.

c} Standard variation of the WSS magnitude WSS. High values are apparent in the true lumen compared to the false lumen.

d} Oscillatory shear index (OSI) on the wall of the computational domain. Areas of high OSI can be found on the posterior wall distal to the entrance tear and at several locations in the false lumen.

from the unsteady simulation; however, information about temporal parameters such as the oWSS or the OSI cannot be derived. The spatial orientation of the WSS magnitude obtained from the steady solution was similar to <WSS> (Figures 4a and 4b), but its absolute values were decreased by a factor of approximately 2.5.

Discussion

The information that can be obtained from CFO simulations comprises a variety of hemodynamic parameters ranging from blood flow velocity over forces exerted on the arterial wall to time averages of directional variations of vectors such as the OSI. The large amount of information conveyed by these parameters has to be tailored to the particular clinical question. Secondary flow patterns, as displayed by the velocity vector, may be indicative of regions where thrombus may form. In particular, a case report of a large basilar aneurysm has successfully linked low velocity magnitude and circulatory flow patterns with the formation of thrombus with fatal outcome.[39] Low and varying WSS magnitude and direction were found to be directly related to the location where a cerebral aneurysm had formed.[40]

Aortic dissections are complex vascular lesions. Conservative medical treatment of B-AO is generally preferred if there are no complications such as rupture, visceral ischemia, or lower limb ischemia at the time of onset.[2] In its initial phase, the therapeutic objective is to normalize blood pressure and lower the left ventricular ejection fraction force using -blockers. Long-term follow-up of these patients includes lifetime medical treatment to minimize aortic wall stress and serial imaging to detect signs of dissection progression, redissection or aneurysmal degeneration, making a surgical intervention necessary.[31]

CFD simulations can provide additional information that may be helpful in therapeutic decision making. Complex flow patterns in the false lumen - as visualized by the blood flow vectors in combination with low velocity magnitudes indicating almost stagnant flow - may be able to predict thrombus formation, even more so if WSS magnitude is low on the aortic wall. All these conditions were present in the investigated B-AO, and the thrombus was actually present in its distal section. Large WSS magnitudes in the true lumen immediately distal to the entrance tear in the described B-AO represent large stresses acting on the endothelial cells, potentially leading to additional damage and tears. The total pressure in the false lumen of a type B II aortic dissection was almost an order of magnitude larger than in the true lumen for maximum inflow. Total pressure in the false lumen calculated from CFD simulations may be able to provide additional information for aortic enlargement. Flow experiments on explanted porcine aortas with artificially created dissections revealed a correlation between enlargement and increased hydrostatic pressure. Most of this increase was due to the increase in the false lumen, and the size of the true lumen remained constant41 To obtain accurate results, the boundary conditions for the CFO simulations have to be realistic. Patient-specific geometries and measured flow rates are essential for obtaining an accurate distribution of the WSS magnitude. The three-dimensional geometry of the lesion can be obtained from a computed

tomographic angiography (CTA) exam or an MRI exam. Flow velocities can be measured noninvasively by Doppler sonography and MRI.

Recently, the accuracy of 2D pcMRI has been established to be approximately 5-10% in the cerebral circulation.[42] MRI is therefore the modality of choice to obtain both geometrical and physiological flow information within one exam. To be of clinical value, the CFO results have to be available to the vascular surgeon before or during the intervention. The results described here were obtained on a dual-core processor PC within four hours by taking advantage of the parallel processing features implemented in the Fluent system. While this time period may be adequate for most cases, a quick overview of the blood flow velocities and the WSS magnitude distribution may be obtained from a steady simulation that can be performed within minutes.

Finally, the CFO results have to be integrated into the clinical workflow. Many vendors of MRI equipment provide a workstation for the post-processing of the acquired MRI images. Ideally, the CFO results should be integrated into this workstation or made available on a separate workstation in the clinical space. It is often not feasible for the surgeon to visit a remotely located research facility.

Limitations

The limitations of the CFO simulations presented here are in the assumptions necessary to simplify the complicated interplay between tissue and blood flow dynamics in-vivo in order to perform computational calculations with the software and computer hardware available today. These include non-slip conditions at the arterial wall, the modeling of blood as a Newtonian fluid, and rigid walls, i.e., no inclusion of fluid structure interactions (FSI). Inclusion of FSI on modeling aortic blood flow has been reported to obtain a more detailed simulation of the blood flow and wall motion.[43-51] For an accurate simulation, however, the mechanical properties of diseased aortic tissue in-vivo (e.g., Young's modulus) have to be known, which is difficult to measure in-vivo for every patient. In addition, CFO combined with FSI is time intensive and may not be able to provide results in a clinical time frame (i.e., in the time from imaging to therapeutic decision making).

Conclusion

Continuous technical advances in the computational simulation of blood flow in-vivo have made it possible to integrate the information obtained with these simulations into the clinical workflow. From the realm of accessible hemodynamic parameters, the ones most pertinent to the clinical question have to be chosen. Fast and accurate boundary conditions are essential for a correct evaluation. Although limitations still exist and are mostly founded in the simplifications necessary to transform the complex human vasculature into a mathematical model, computational simulations have the potential of enhancing standard medial images, thus aiding therapeutic decision making.

References

1. Bergan JJ, Yao JST, editors. Aneurysms: Diagnosis and Treatment. New York: Grune & Stratton, Inc.; 1982.
2. Onitsuka S, Akashi H, Tayama K, Okazaki T, Ishihara K, Hiromatsu S, Aoyagi S. Long-term outcome and prognostic predictors of medically treated acute type B aortic dissections. Ann Thorac Surg. 2004 Oct;78(4):1268-73.
3. Ince H, Nienaber CA. Diagnosis and management of patients with aortic dissection. Heart. 2007 Feb;93(2): 266-70.
4. Eagle KA, DeSanctis RW. Aortic dissection. Curr Probl Cardiol. 1989 May;14(5):225-78.
5. Kamalakannan D, Rosman HS, Eagle KA. Acute aortic dissection. Crit Care Clin. 2007 Oct;23(4):779-800, vi.
6. Smith AD, Schoenhagen P. CT imaging for acute aortic syndrome. Cleve Clin J Med. 2008 Jan;75(1):7-9, 12, 15-17 passim.
7. Lin J, Chen B, Wang JH (2006) Diagnosis of systemic arterial diseases with whole-body 3 0 contrast-enhanced magnetic resonance angiography. Chin Med J (Engl). 2006 Nov 5;119(21):1772-8.
8. Guthaner OF, Miller D C Digital subtraction angiography of aortic dissection. AJR Am J Roentgenol. 1983 Jul;141(1):157-61.
9. Myerowitz PD, Swanson DK, Turnipseed WD. Applications of digital subtraction angiography in cardiovascular diagnosis. Surg Clin North Am. 1985 Jun;65(3):423-37.
10. Xu SD, Huang FJ, Du JH, Li Y, Fan ZM, Yang JF, Yu XY, Zhang ZG. A study of aortic dimension in type B aortic dissection. Interact Cardiovasc Thorac Surg. 2008 Apr;7(2):244-8.
11. Scott R, Atkins F, Harper PV. Median Window Filter as a Smoothing-Edge Preserving Technique. J Nucl Med. 1978;19 (6) :749-749.

12. Karmonik C, Bismuth JX, Davies MG, Lumsden AB. Computational hemodynamics in the human aorta: a computational fluid dynamics study of three cases with patient-specific geometries and inflow rates. Technol Health Care. 2008;16(5): 343-54.

13. Minami H, Sugimoto T, Okada M. Evaluation of acute aortic dissection by cine-MRI. Kobe J Med Sci. 1999 Feb;45(1):1-11.

14. Wedding KL, Draney MT, Herfkens RJ, Zarins CK, Taylor CA, Pelc NJ. Measurement of vessel wall strain using cine phase contrast MRI. J Magn Reson Imaging. 2002 Apr;15(4):418-28.

15. Draney MT, Herfkens RJ, Hughes TJ, Pelc NJ, Wedding KL, Zarins CK, Taylor CA. Quantification of vessel wall cyclic strain using cine phase contrast magnetic resonance imaging. Ann Biomed Eng. 2002 Sep;30(8):1033-45.

16. Draney MT, Arko FR, Alley MT, Markl M, Herfkens RJ, Pelc NJ, Zarins CK, Taylor CA. Quantification of vessel wall motion and cyclic strain using cine phase contrast MRI: in vivo validation in the porcine aorta. Magn Reson Med. 2004 Aug;52(2):286-95.

17. Frydrychowicz A, Markl M, Harloff A, Stalder AF, Bock J, Bley TA, Berger A, Russe MF, Schlensak C, Hennig J, Langer M. {Flow-sensitive in-vivo 4D MR imaging at 3T for the analysis of aortic hernodynarnics and derived vessel wall parameters]. Rofo. 2007 May;179(5):463-72.

18. Hope TA, Markl M, Wigstrom L, Alley MT, Miller DC, Herfkens RJ. Comparison of flow patterns in ascending aortic aneurysms and volunteers using four-dimensional magnetic resonance velocity mapping. J Magn Reson Imaging. 2007 Dec;26(6):1471-9.

19. Yamashita S, Isoda H, Hirano M, Takeda H, Inagawa S, Takehara Y, Alley MT, Markl M, Pelc NJ, Sakahara H. Visualization of hemo-$d_{y\,n}$arnics in intracranial arteries using time-resolved three-dimensional phase-contrast MRI. J Magn Reson Imaging. 2007 Mar;25(3): 473-8.

20. Berstein MA, King KF, Zhou XJ. Handbook of MRI Pulse Sequences. Burlington, MA: Elsevier Academic Press; 2004.

21. NHLBI: Division of Cardiovascular Diseases {Internet]. Bethesda, MD: National Heart, Lung, and Blood Institute; c2006. Division of Cardiovascular Diseases Strategic Plan; 2008 Sep [cited 2009 Jun 25]. Available from: http://www.nhlbi.nih.gov/about/dcvd/sp/.

22. Patterson GS Jr. Prospects for Computational Fluid-Mechanics. Annual Review of Fluid Mechanics. 1978;10:289-300.

23. Barnes RW. Hemodynamics for the vascular surgeon. Arch Surg. 1980 Feb;l15(2): 216-23.

24. Graves RA Jr. Computational Fluid Dynamics: The Coming Revolution. Astronautics & Aeronautics. 1982 Mar;20(3):20-8.

25. Lou Z, Yang WJ. A computer simulation of the blood flow at the aortic bifurcation. Biomed Mater Eng. 1991;1(3):173-93.

26. Lou Z, Yang WJ. A computer simulation of the blood flow at the aortic bifurcation with flexible walls. J Biomech Eng. 1993 Aug;115(3): 306-15.

27. Kumar BV, Naidu KB. Finite element analysis of nonlinear pulsatile suspension flow dynamics in blood vessels with aneurysm. Comput Biol Med. 1995 Jan;25(1):1-20.

28. Foutrakis GN, Burgreen G, Yonas H, Sclabassi RJ. Construction of 3-D arterial volume meshes from magnetic resonance angiography. Neurol Res. 1996 Aug;18(4): 354-60.

29. Long Q, Xu XY, Bourne M, Griffith TM. Numerical study of blood flow in an anatomically realistic aorto-iliac bifurcation generated from MRI data. Magn Reson Med. 2000 Apr;43(4):565-76.

30. Di Martino ES, Guadagni G, Fumero A, Ballerini G, Spirito R, Biglioli P, Redaelli A. Fluid-structure interaction within realistic three-dimensional models of the aneurysmatic aorta as a guidance to assess the risk of rupture of the aneurysm. Med Eng Phys. 2001 Nov;23(9):647-55.

31. Wood NB, Weston SJ, Kilner PJ, Gosman AD, Firmin DN. Combined MR imaging and CFD simulation of flow in the human descending aorta. J Magn Reson Imaging. 2001 May;13(5):699-713.

32. Leuprecht A, Perktold K, Kozerke S, Boesiger P. Combined CFD and MRI study of blood flow in a human ascending aorta model. Biorheology. 2002;39(3-4): 425-9.

33. Steinman DA. Image-based computational fluid dynamics: a new paradigm for monitoring hemodynamics and atherosclerosis. Curr Drug Targets Cardiovasc Haematol Disord. 2004 Jun;4(2):183-97.

34. Karmonik C, Klucznik R, Benndorf G. Blood flow in cerebral aneurysms: comparison of phase contrast magnetic resonance and computational fluid $d_{y\,n}$amics--preliminary experience. Rofo. 2008 Mar;180(3):209-15.

35. Karmonik C, Klucznik R, Benndorf G. Comparison of velocity patterns in an ACom.A aneurysm measured with 2D phase contrast MRI and simulated with CFO. Technol Health Care. 2008;16(2):119-28.

36. Malek AM, lzumo S. Control of endothelial cell gene expression by flow. J Biomech. 1995 Dec;28(12):1515-28.

3Z Abramoff MD, Magelhaes PJ, Ram SJ. Image Processing with ImageJ. Biophotonics International. 2004;11(7):36-42.

38. He XJ, Ku DN. Pulsatile flow in the human left coronary artery bifurcation: average conditions. Journal of Biomechanical Engineering-Transactions of the ASME. 1996;118:74-82.

39. Jou LD, Wong G, Dispensa B, Lawton MT, Higashida RT, Young WL, Saloner D. Correlation between lumenal geometry changes and hemodynamics in fusiform intracranial aneurysms. AJNR Am J Neuroradiol. 2005 Oct;26(9):2357-63.

40. Mantha A, Karmonik C, Benndorf G, Strother C, Metcalfe R. Hemodynamics in a cerebral artery before and after the formation of an aneurysm. AJNR Am J Neuroradiol. 2006 May;27(5):1113-8.

41. Williams DM, LePage MA, Lee DY. The dissected aorta: part I. Early anatomic changes in an in vitro model. Radiology. 1997 Apr;203(1):23-31.

42. Zhao M, Amin-Hanjani S, Ruland S, Curcio AP, Ostergren L, Charbel FT. Regional cerebral blood flow using quantitative MR angiography. AJNR Am J Neuroradiol. 2007 Sep;28(8):1470-3.

43. Gao F, Ohta 0, Matsuzawa T. Fluid-structure interaction in layered aortic arch aneurysm model: assessing the combined influence of arch aneurysm and wall stiffness. Australas Phys Eng Sci Med. 2008 Mar;31(1):32-41.

44. Kleinstreuer C, Li Z, Farber MA. Fluid-structure interaction analyses of stented abdominal aortic aneurysms. Annu Rev Biomed Eng. 2007;9:169-204.

45. Leung JH, Wright AR, Cheshire N, Crane J, Thom SA, Hughes AD, Xu Y. Fluid structure interaction of patient specific abdominal aortic aneurysms: a comparison with solid stress models. Biomed Eng Online. 2006 May 19;5:33.

46. Li Z, Kleinstreuer C. Fluid-structure interaction effects on sac-blood pressure and wall stress in a stented aneurysm. J Biomech Eng. 2005 Aug;127(4):662-71.

47. Li Z, Kleinstreuer C. Blood flow and structure interactions in a stented abdominal aortic aneurysm model. Med Eng Phys. 2005 Jun;27(5):369-82.

48. Li Z, Kleinstreuer C. Computational analysis of type II endoleaks in a stented abdominal aortic aneurysm model. J Biomech. 2006;39(14): 2573-82.

49. Li Z, Kleinstreuer C. Analysis of biomechanical factors affecting stent-graft migration in an abdominal aortic aneurysm model. J Biomech. 2006;39(12):2264-73.

50. McGregor RH, Szczerba D, Szekely G. A multiphysics simulation of a healthy and a diseased abdominal aorta. Med Image Comput Comput Assist Interv Int Conf Med Image Comput Comput Assist Interv. 2007;10(Pt 2):227-34.

51. Pelerin JL, Kulik C, Goksu C, Coatrieux JL, Rochette M. Fluid/structure interaction applied to the simulation of Abdominal Aortic Aneurysms. Conf Proc IEEE Eng Med Biol Soc. 2006;1:1754-7.